

Photovoltaic Recovery of All Printable Mesoporous-Carbon-based Perovskite Solar Cells

Stav Alon, Maayan Sohmer, Chandra Shakher Pathak, Iris Visoly-Fisher, and Lioz Etgar*

Lead halide perovskites attract much attention in recent years as a realistic solution for efficient and low-cost solar cells. One of the interesting solar cell structures is the fully mesoporous-carbon-based perovskite solar cells. The mesoporous layers can be fabricated entirely by screen printing with the potential for upscaling. Herein, the two-step deposition of perovskite in mesoporous-carbon-based perovskite solar cells is studied. The influence of the dipping time on the photovoltaic parameters is investigated using charge extraction and intensity-modulated photovoltage spectroscopy (IMVS) measurements. A power conversion efficiency of 15% is observed for cells fabricated using two-step deposition which is one of the highest reported for this solar cell structure. Stability characterizations at maximum power point (MPP) tracking show degradation with time, however a complete recovery of the devices in the dark is revealed. Analyzing the mechanism for this shows that the perovskite's unit cell shrinks during the recovery process due to internal stress relief. This interesting phenomenon opens the possibility to optimize the stability of these solar cells for commercial applications.

1. Introduction

Perovskite solar cells demonstrated a significant progress in their power conversion efficiency (PCE) since its first use as a light harvester in 2009.^[1] The lead halide perovskites contain 3D arrays of inorganic PbX_6 anions surrounded by organic or inorganic counter ions (for example, Cs^+).^[2] The lead halide perovskite exhibits a large absorption coefficient, long-range photocarrier diffusion lengths, and a suitable bandgap in the


visible range.^[3–6] Hybrid perovskites can be used in several solar cells architectures such as mesoporous, planar, inverted, and even without hole transport material (HTM).^[3,7–9] The elimination of HTM can lower the cost of the solar cell and simplify its fabrication process. An interesting HTM free solar cell structure is based on a mesoporous carbon electrode. In this solar cell architecture, the perovskite is deposited at the last step and penetrates through the whole mesoporous structure (see Figure 1a).^[10] Mesoporous-carbon-based perovskite solar cells (mC-PSCs) have several unique features making them an attractive solar cell structure and a good candidate for commercialization. They can be fabricated using fast and simple processes such as screen printing, moreover they do not require an evaporation of the cathode making them a low-cost technology.^[11] The elimination of a metallic back electrode is expected to have

significant advantages for the photostability of such cells, as the well-documented metal-induced degradation mechanism^[12–14] is prevented. Indeed, mC-PSCs have previously demonstrated impressive photostability^[15–18] with embedded MAPbI_3 with ammoniumvaleric acid (AVA)-based additives. Stability studies of mC-PSCs therefore allow studying intrinsic stability, degradation, and recovery phenomena, which are not masked by the metal contact-related ones.

Over the past years, mC-PSCs demonstrated an increase in their PCE achieving up to 16% efficiency.^[19,20] A major concern in these mC-PSCs is how to achieve complete and uniform penetration of the perovskite through the porous structure which usually has a thickness of several micrometers. Toward that end, several reports modified the perovskite composition, while others changed the perovskite's precursor solution.^[19,21–24] There are two common ways to deposit the perovskite, i.e., one-step and two-step methods. In the one-step deposition, the perovskite's precursors are mixed in one solution, whereas in the two-step deposition first the lead halide is dropped over the electrode, and in the second step, the cell is dipped into the cations' solution.^[10,25,26] In carbon-based perovskite solar cells, the one-step deposition is more frequently used^[21,22,24,27] compared with the two-step deposition.^[28,29] The use of two-step deposition can be advantageous for mC-PSCs as there are more options for selection of solvents for the deposition, better control

S. Alon, M. Sohmer, Prof. L. Etgar
Institute of Chemistry
The Center for Nanoscience and Nanotechnology
Casali Center for Applied Chemistry
The Hebrew University of Jerusalem
Jerusalem 91904, Israel
E-mail: lioz.etgar@mail.huji.ac.il

Dr. C. S. Pathak, Prof. I. Visoly-Fisher
Department of Solar Energy and Environmental Physics
Swiss Institute for Dryland Environmental and Energy Research
Jacob Blaustein Institutes for Desert Research
Ben-Gurion University of the Negev
Midreshet Ben-Gurion 8499000, Israel

 The ORCID identification number(s) for the author(s) of this article can be found under <https://doi.org/10.1002/solr.202100028>.

DOI: 10.1002/solr.202100028

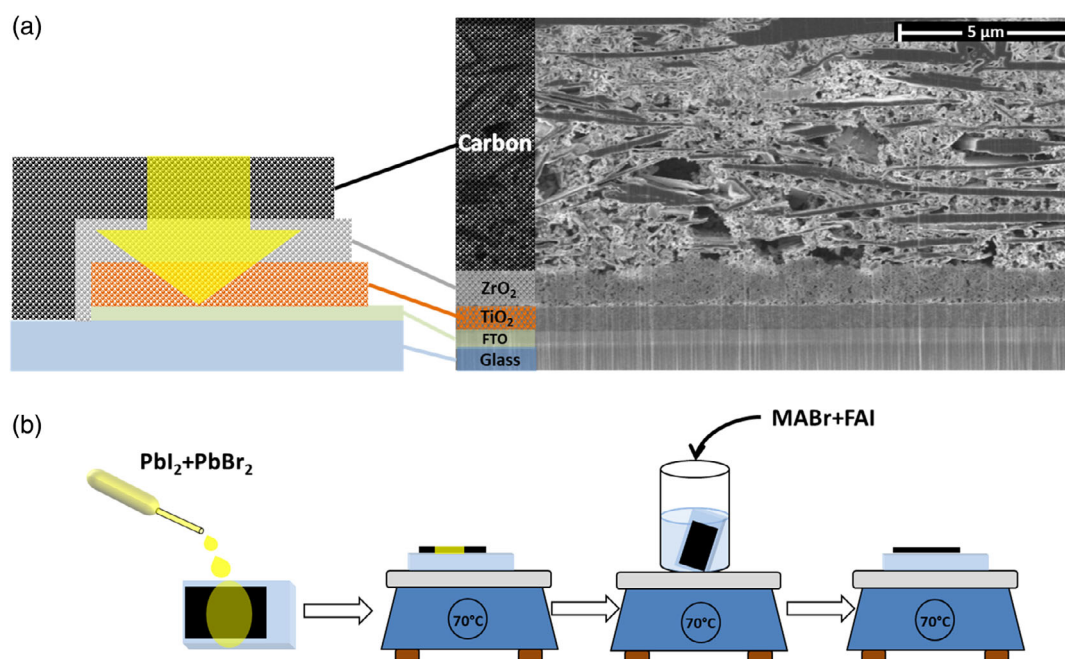


Figure 1. a) Schematic description of the mesoporous carbon perovskite-based solar cells structure and its scanning electron microscope-focused ion beam cross-sectional image. b) Schematic illustration of the two-step deposition process. The first stage includes dropping of the $\text{PbI}_2 + \text{PbBr}_2$ solution, the second step includes dipping into the cation solution of $\text{FAI} + \text{MABr}$.

over the pore filling, which is critical in this solar cell structure, and improved reproducibility.^[30,31] It allows better control of the perovskite morphology for improved cell performance, compared with one-step deposition,^[32–34] and the development of stable Sn-based perovskite solar cells (PSCs).^[35] Our work has previously demonstrated that two-step deposited mC-PSCs undergo a shorter “maturation process” after fabrication, and allow increased crystalline orientation of the perovskite, compared with one-step deposited mC-PSCs.^[28] The two-step deposition was also recently utilized for the fabrication of all-inorganic mC-PSCs with exceptional stability,^[36] further demonstrating the significance of this fabrication method.

In this work, we concentrate on achieving highly efficient mC-PSCs using the two-step deposition process of the perovskite. We modified several parameters during the deposition process achieving 15% efficiency. Charge extraction (CE) and intensity-modulated photovoltage spectroscopy (IMVS) measurements were used to elucidate the detailed photovoltaic (PV) mechanism of those cell structures. Stability measurements under maximum power point (MPP) tracking reveal significant recovery of the PV parameters after 1 day in the dark. The mechanism for this recovery is discussed in detail.

2. Results and Discussion

Figure 1a shows the structure of the mC-PSC. The cell's structure includes $\approx 0.7 \mu\text{m}$ mesoporous TiO_2 which acts as an electron transport material (ETM), $\approx 9 \mu\text{m}$ of mesoporous carbon which act as the cathode, and $\approx 1 \mu\text{m}$ of intermediate mesoporous ZrO_2 which prevent a direct contact between the TiO_2

and the carbon. The perovskite penetrates through all device layers from the top to the bottom. Figure 1a shows a cross section made by focused ion beam (FIB) milling of this solar cell where all the layers can be observed. Upon illumination from the glass side, electrons and holes are generated in the perovskite where electrons are injected to the TiO_2 and holes are collected by the carbon electrode.

Here, we concentrate on two-step deposition for the mC-PSC where we studied the effect of the different deposition parameters on the PV performance and stability. $\text{MA}_{0.15}\text{FA}_{0.85}\text{Pb}(\text{I}_{0.85}\text{Br}_{0.15})_3$ perovskite was used for this study (FA- formamidinium, MA-methyl ammonium). This perovskite composition was chosen as it is one of the compositions that show high PV performance in perovskite solar cells.^[37,38] As in this study we investigate the two-step deposition process, it was not possible to add Cs^+ cation to the perovskite composition due to the fact that the Cs^+ cation cannot be dissolved in the dipping cation solution without the presence of lead halide. The absorbance of this perovskite composition is presented in Figure S1, Supporting Information, where the formamidinium shifts the bandgap absorption edge to wavelength of over 800 nm. The two-step process is shown in Figure 1b, briefly a drop of lead halide solution is placed on the active area followed by annealing, then the cell is dipped into the cation solution for a certain dipping time. The crystallization of the perovskite is finalized by an annealing step. No antisolvent treatment is used in the deposition process.

Initially, to find the optimized conditions for this study, we varied the solution's concentration of the first step (Pb halide solution in dimethylformamide(DMF):dimethyl sulfoxide [DMSO]), whereas the second step (i.e., dipping) remained

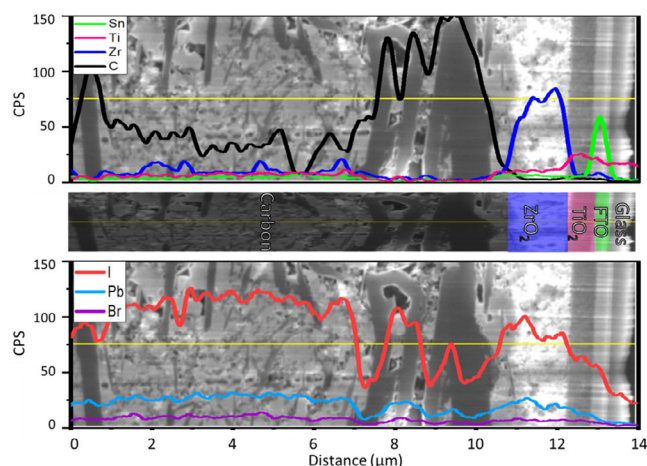


Figure 2. EDS measurements of a cross-sectional lamella of the cell made by FIB milling. The various elements are indicated in different colors in the figure.

constant. The solution of the first step was composed of PbI_2 and PbBr_2 at a weight ratio of 85:15 in DMF:DMSO (85:15 vol%) mixture. Three different concentrations were studied, 1, 1.5, and 2 M (Table S1, Supporting Information). The 2 M achieved the best results in all PV parameters; this concentration is relatively high related to standard two-step deposition processes. The reason for that lies in the thickness of the device, where the perovskite has to penetrate several micrometers (see Figure 1a, 2) and high concentration can guarantee that.

Next, we varied the Br concentration in the perovskite. It is well known that the bromide content affects the perovskite bandgap, as more bromide shifts the bandgap to the blue region.^[39] The Br concentration was varied between 0% (full iodide) to 25% of the halide content, as shown in Table S2, Supporting Information. A high open-circuit voltage (V_{oc}) can be observed with high Br concentrations of 10% and 15%, moreover the current density (J_{sc}) is also increased in these cases compared with other concentrations. The best performance in this case was achieved for 15% Br. Interestingly, even though the 15% Br concentration is supposed to increase the perovskite bandgap, the J_{sc} is still increased. As reported earlier, at low Br concentrations, the band gap is not altered, as the bromides fill vacancies and traps in the perovskite crystal, therefore they do not affect the bandgap.^[40]

Based on these optimized parameters, we modified the dipping time in the second step of the deposition. This parameter should have a major influence on the PV performance of the

mC-PSC as the cell structure consists of several micrometers of mesoporous scaffold where the perovskite has to penetrate through it. The dipping time is a critical parameter, as it determines the time which is required for the perovskite solution to penetrate along the porous scaffold without crystallizing on the way. The dipping solution contains formamidinium iodide (FAI) and methylammonium bromide (MABr) at a weight ratio of 85:15 in isopropyl alcohol (IPA).

Table 1 shows the PV parameters of cells fabricated with four different dipping times, whereas their corresponding current density–voltage (JV) curves are shown in Figure 3a. It can be seen that 20 min dipping achieve the best PV performance with an average efficiency of 13.3% and champion cell of 15% efficiency, one of the highest reported for this solar cell structure. Too short dipping time (5 min) was not enough for the perovskite to penetrate through the pores and to convert the PbI_2 and PbBr_2 to perovskite. On the other hand, if the dipping time was too long, such as 45 and 90 min, a slight reduction in the PV parameters was also observed, which is supported by the X-ray diffraction (XRD) measurements as discussed in the following sections. A typical hysteresis characterization of the cells is shown in Figure S2, Supporting Information, the hysteresis is small with almost no change in the V_{oc} and a calculated hysteresis index of 0.153. Figure 3d shows the change in the PV parameters as a function of the mask size (absolute values are indicated in Table S3, Supporting Information). There is no change between 0.09 and 0.1 cm^2 mask size, all the PV parameters are preserved. Increasing the mask size to 0.16 cm^2 does not affect the V_{oc} and the FF; however, the J_{sc} drops and as a result the efficiency. In the case of large active areas, the sheet resistance of the electrodes is more pronounced, which results in resistivity losses that affect the J_{sc} of the cell.^[41]

An energy dispersive X-ray spectroscopy (EDS) line scan made on a thin lamella fabricated by FIB-milled cross section of the solar cell shows the relevant elements of the perovskite through the whole device structure (Figure 2). Iodine, bromine, and lead can be found from the top to the bottom layers. The iodide concentration is higher than the bromide as indicated by the EDS which supports the studied perovskite composition. This indicates that in order for the solar cell to operate efficiently, full penetration of the perovskite is necessary. Therefore, we can assume that in the case of low PV parameters incomplete penetration of the perovskite might be the reason.

To get better understanding of the PV mechanism of this solar cell structure fabricated at various dipping times, CE and IMVS measurements were carried out. CE measurements can shed light on the rate of recombination in our devices. The CE measurement is conducted under open-circuit conditions,

Table 1. PV parameters of cells fabricated with different dipping times. In brackets is the average values of 30 cells, the values outside the brackets are of the champion cell for each fabrication process.

Dipping time	V_{oc} [V]	J_{sc} [mA cm^{-2}]	FF [%]	E_{ff} [%]
5	0.87 (0.84 ± 0.06)	16.4 (11.2 ± 3.9)	56.2 (60 ± 3)	8.0 (5.6 ± 2.0)
20	0.93 (0.91 ± 0.04)	23.6 (22.8 ± 0.9)	68 (64 ± 3)	15.01 (13.3 ± 0.8)
45	0.90 (0.89 ± 0.03)	23.8 (21.0 ± 2.4)	64.9 (63 ± 4)	13.94 (11.7 ± 1.0)
90	0.88 (0.88 ± 0.04)	20.3 (18.1 ± 1.8)	65.7 (65 ± 5)	11.71 (10.4 ± 0.9)

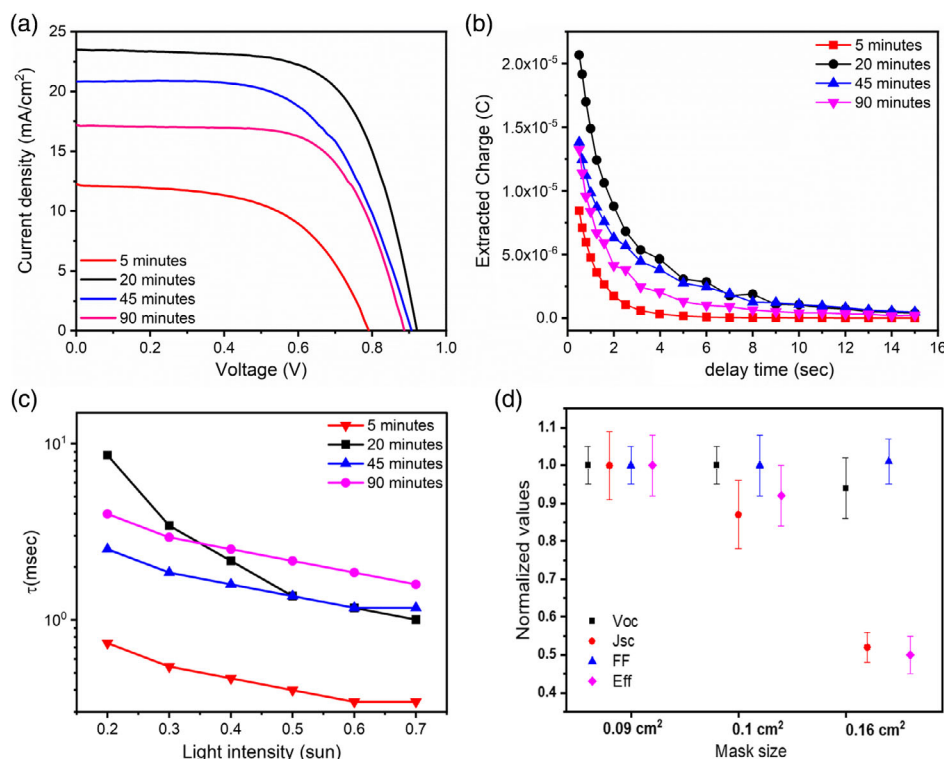


Figure 3. The effects of different dipping times on the cell properties. a) *J/V* curves. b) CE measurements. c) IMVS. d) PV parameters as a function of the mask size.

where the device is illuminated for 5 s then the light is switched off and the internal charge carrier density decays for a varied period of time (delay time). Finally the remaining charge carriers are extracted when the device is short circuited. Therefore, in the case of long delay time, there are less charge carriers to be extracted. As long as there are more charge carriers left for a specific delay time, one can assume that the rate of recombination is slower than other devices at the same delay time. Figure 3b shows that in the case of cells fabricated at 20 min dipping the rate of recombination is the slowest, whereas in the case of 5 min dipping the highest recombination rate was observed. These results correlate well with the PV parameters shown in Table 1.

In addition to the CE measurements, IMVS measurements were carried out. Using IMVS, it is possible to get indication of the carrier lifetime in the different devices (fabricated at different dipping times) which are associated with the charge carrier's recombination. Figure 3c shows the lifetime for the different cells as a function of the light intensity. In the case of cells fabricated at 5 min dipping time, the lifetime is shorter than in cells fabricated at other dipping times for the whole range of light intensities. This shows a higher charge carrier recombination, which is correlated with the lower PV parameters in this case as compared with the other cases. Probably, the 5 min dipping time is too short for full conversion of the perovskite throughout the entire device thickness.

An interesting point from the IMVS is related to cells fabricated at 90, 45, and 20 min dipping times. In the case of cells

fabricated at 90 and 45 min dipping time the lifetime is almost not affected by the light intensity, in contrast to the cells fabricated at 20 min dipping time where the lifetime decreased with increased light intensity. Previously, we reported^[42] on such a behavior in perovskite solar cells which was related to charge accumulation at the interfaces between the layers. Based on that, it can be assumed that in the case of cells fabricated at 20 min dipping there is less charge accumulation at the interfaces, therefore a higher current density is achieved compared with the other cases.

XRD measurements were carried out for the different cells, as shown in Figure 4a. Focusing on the peak at 12.8° (Figure 4b), which is associated with residual PbI₂, it can be seen that the intensity decreased with the dipping time. A high amount of PbI₂ is left after 5 min of dipping as a result of incomplete conversion of the perovskite; this is further supported by our observations from the IMVS. Still in the case of cells fabricated with 20, 45, and 90 min dipping time, there is some residual PbI₂. As reported previously, a small amount of PbI₂ contributes to the PV performance by preventing defects at the perovskite grain boundaries, therefore reducing the losses associated with recombination.^[43,44] This can explain the PV performance variations with the various dipping times.

Figure 4c shows the peak position and full width half maximum (FWHM) of the peak at 14°, which is related to the (110) plane of tetragonal methyl ammonium lead iodide perovskite. As indicated in the figure, the peak position did not change following different dipping times. However, the FWHM is

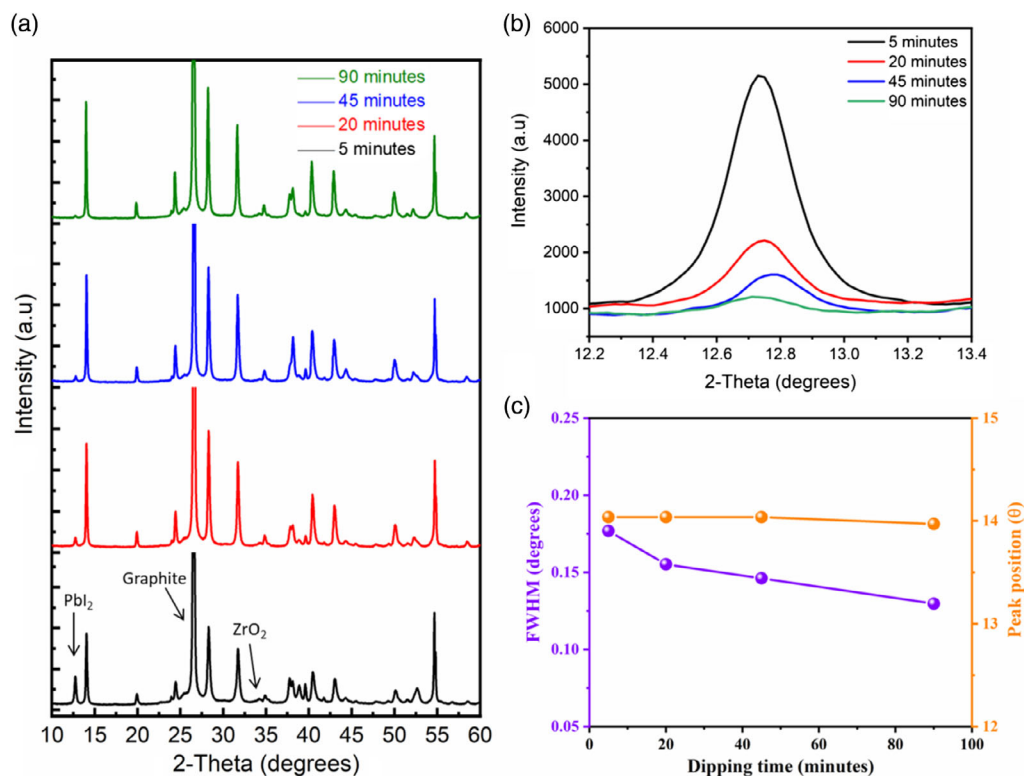


Figure 4. a) XRD measurements of cells fabricated at different dipping times. The graphite peak is very intense; therefore, it was shortcut at the end. b) Magnification of the PbI₂ XRD peak at $\approx 12.8^\circ$. c) Peak position and the FWHM for the 14° peak as a function of the dipping time.

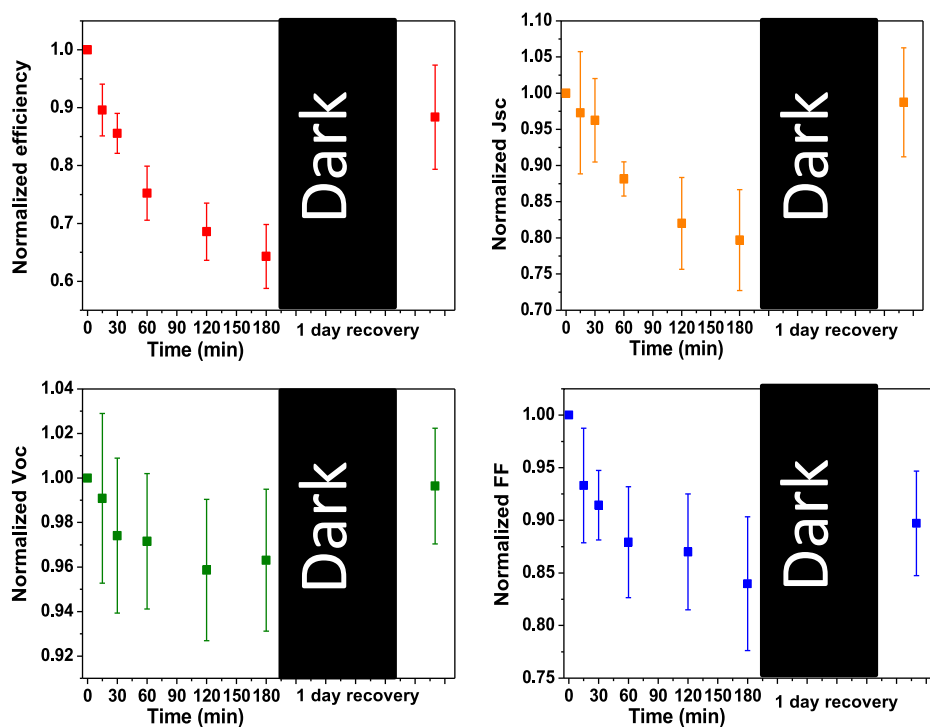


Figure 5. Variation of normalized PV parameters (averaged for four devices) under 1 sun illumination at MPP tracking under nitrogen environment followed by recovery in the dark for 1 day.

reduced with longer dipping times. The main drop in FWHM occurs between 5 and 20 min. Following longer dipping times, the reduction in the FWHM is more moderate. The reduction in the FWHM indicates improved crystallinity, which correlates with the PV performance of these cells.

Stability studies of mC-PSCs were conducted toward understanding intrinsic perovskite stability, degradation, and recovery phenomena, at the absence of metal contact-induced degradation. The stability measurements were carried out outdoor under natural 1 sun illumination using MPP tracking in sealed N₂ environment or in ambient (Figure 5 and Figure S3, Supporting Information). *JV* curves were measured 6 times during 3 h of stressing, followed by 1-day recovery in the dark. Figure 5 shows that all the PV parameters decreased after three outdoor exposure hours at MPP, with a PCE average decrease to $\approx 65\%$ of its initial value. This relatively fast degradation is attributed to the type of perovskite used as absorber herein, MA_{0.15}FA_{0.85}Pb(I_{0.85}Br_{0.15})₃, as it is not stabilized by Cs addition.^[45] The PCE decrease is correlated with the decrease in *J*_{sc}, which is the most significantly affected PV parameter (Figure 5), probably indicating initial perovskite intrinsic degradation. Indeed, variations of the perovskite-related XRD peaks show small decrease in peak intensities after 3 h of light exposure (after normalization of all diffractograms to the graphite peak intensity, Figure 6b–e). Similar patterns in PV parameter variations were observed during air stressing outdoors, though the extent of degradation was much

larger after 3 stressing hours: PCE decreased to about 25% and *J*_{sc} decreased to $\approx 30\%$ of their initial values (Figure S3, Supporting Information).

However, our main interest was in the outstanding recovery demonstrated by all cells within 1 day in the dark (Figure 3 and 5). Figure 5 shows that the efficiency of cells stressed in N₂ recovered to 94% of its initial value, the *V*_{oc} recovered to 98% of its initial value, the FF recovered to 95% of its initial value, where the *J*_{sc} recovered completely to its initial value. mC-PSCs stressed in ambient recovered to $65 \pm 15\%$ of their initial PCE and *J*_{sc}. The smaller extent of recovery in ambient-stressed cells is probably due to nonreversible perovskite reaction with humidity and oxygen, which is hampered by the hydrophobic graphite but not completely eliminated. Indeed, superoxide formation was demonstrated in ambient photostressing of mC-PSCs, at a slower rate compared with perovskite on mesoporous metal-oxide substrates likely thanks to inhibition of moisture penetration by the carbon layer.^[46] It was already reported that N₂-protected mC-PSCs can recover in the dark,^[47] however, the mechanism was not studied in details. The almost complete recovery of the PV parameters after 1 day in the dark is unique for this cell structure, whereas for a standard perovskite solar cell architecture, the extent of recovery is typically more limited, especially at later stages of cell performance degradation.^[48] The impressive recovery in *J*_{sc} hints to intrinsic recovery of the perovskite.

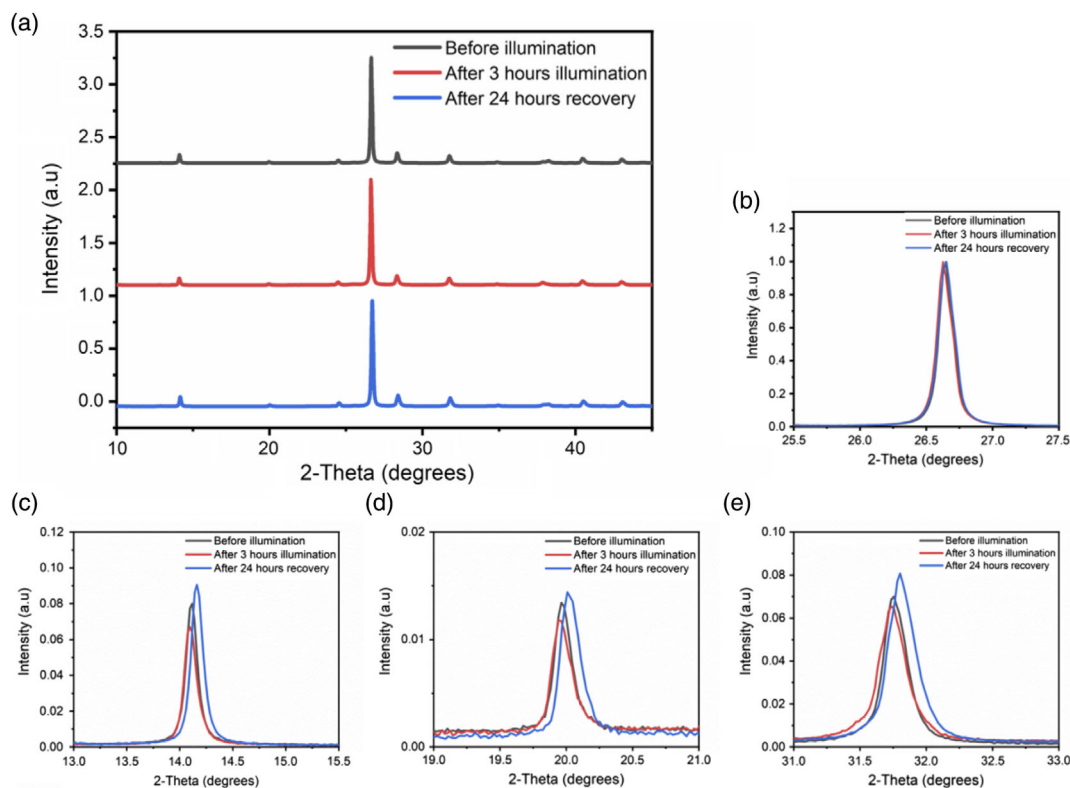


Figure 6. a) XRD of the same cell before illumination, after 3 h of illumination, and after 24 h recovery in the dark. b) Magnification of the peaks at 2θ of 26.6° related to graphite peak; c) Magnification of the peaks at 2θ of 14.1° related to perovskite (001) planes; d) Magnification of the peaks at 2θ of 20.0° related to perovskite (011) planes, and e) Magnification of the peaks at 2θ of 31.8° angle related to perovskite (012) planes. The peak intensities were normalized with respect to the carbon peak, which was assumed to be constant in all XRD measurements.

XRD measurements were carried out before illumination, after 3 h of illumination and after 24 h of recovery in the dark (Figure 6), to study the perovskite structure following stressing and recovery. A shift in perovskite-related peak positions to larger angles is observed, accompanied by peak intensity increase, following the recovery stage (Figure 6c–e). A shift of several tenths of degrees, as observed here, is well above the step size of the technique, i.e., its resolution limit. The shift to larger angles indicates the contraction of the crystalline unit cell. Such contraction may be related to relaxed tensile stresses in the perovskite. Indeed, tensile stresses were previously detected in as-processed perovskite films as a result of the thermal treatment during film fabrication,^[49,50] as used also herein. We therefore propose that partial perovskite decomposition and recrystallization occur within the carbon electrode pores during light exposure and subsequent dark recovery, respectively, relieving internal stresses in the perovskite. We note that ion migration and trap formation were previously suggested to account for perovskite recovery,^[37] and could not be ruled out. However, it is hard to believe that such mechanisms can account for the observed decrease and subsequent increase in XRD peak intensities, as well as the observed changes in the crystalline dimensions. If the contraction in dimensions is to be related to ion out-migration, recovery should result in subsequent increase in these dimensions and return to the original XRD peak position, which is not observed.

Recrystallization can occur when the perovskite's components are in close proximity to each other,^[51,52] and was previously shown in mC-PSCs exposed to prolonged humidity-assisted heat treatment.^[53] As the solar cell structure is composed of mesoporous networks which keep the distance between the perovskite components close even after decomposition, recrystallization in the pores is feasible. Comparison of the XRD peak intensities supports this hypothesis: the perovskite-related peak intensities decrease following degradation and increase during recovery (Figure 6). As internal stresses are known to negatively affect PSC stability,^[50] such degradation–recovery cycles inducing stress relief may contribute to improved device operational stability. We postulate that this explains the discrepancy between fast degradation observed under continuous illumination and relative stability at outdoor measurements of mC-PSCs described by De Rossi et al.^[47] Our characterization therefore suggests that degradation–recrystallization cycles may sometimes be beneficial for mC-PSC operational stability, and further highlights the importance of light cycling in PSC stability measurements.^[54]

3. Conclusion

In this work, we study two-step perovskite deposition in all-printable mC-PSCs. By modifying the perovskite precursors' concentration and the dipping time, a PCE of 15% was achieved. The dipping time in the perovskite deposition of this solar cell structure is critical due to its thickness and mesoporous structure. CE and IMVS show a lower recombination rate and longer carrier lifetime for cells fabricated with dipping time of 20 min.

An interesting observation was revealed in stability characterization. The cells showed almost complete recovery in all PV parameters after their degradation in N₂, and impressive recovery also after degradation in ambient. The close proximity of the

perovskite's components within the mesoporous carbon structure assist the recovery process in this case, as was observed by XRD measurements. We propose that partial perovskite decomposition and recrystallization occur within the carbon electrode pores during light exposure and subsequent dark recovery, respectively, relieving internal stresses in the perovskite. As internal stresses are known to negatively affect PSC stability, such degradation–recovery cycles inducing stress relief may contribute to improved device operational stability.

4. Experimental Section

Materials and Solvents: Hellmanex III, titanium diisopropoxide bis(acetylacetonate) (75% wt. in isopropanol), lead iodide (99%), *N,N*-dimethylformamide (anhydrous 99.8%), and isopropyl alcohol (anhydrous 99.5%) were purchased from Sigma-Aldrich. Formamidinium iodide (FAI), methylammonium bromide (MABr), and TiO₂ paste (90T) were purchased from GreatCell Solar Company. Titanium (IV) chloride (TiCl₄) was purchased from Wako. Zr-nanoxide ZT/SP (46411) was purchased from Solaronix. Ethanol absolute (99.5%) and DMSO (99.7% extra dry) were purchased from Acros Organics. A hyperthermic conductive carbon paste was purchased from FEIMING Chemical Ltd. All perovskite precursors and anhydrous solvents were kept in a nitrogen-filled glovebox.

Device Preparation: A fluorine-doped tin oxide (FTO)-coated glass etched by laser to disconnect the anode and cathode sides was used as the substrate. The glass substrates were cleaned and sonicated for three cycles of 30 min in soap, Hellmanex 1%, and a mix of ethanol and acetone in water. After that, the glass was treated in oxygen plasma for 10 min. Next, the substrates were spin coated with a 13.3% solution of titanium diisopropoxide bis(acetylacetonate) in ethanol absolute (5000 rpm, 30 s) and annealed on a hot plate (30 min, 450 °C). After cooling down, the substrates were treated by dipping in a water-based TiCl₄ solution (1.6 mL TiCl₄ 150 mL triple distilled water) and transferred into an oven at 70 °C for 30 min and then washed, dried, and annealed at 450 °C for 30 min. After cooling again, TiO₂ paste was screen printed using a 130 mesh polymer screen and sintered at 500 °C for 30 min on a hot plate. Then, the same process of TiCl₄ treatment was repeated. Next, ZrO₂ paste was screen printed using a 130 mesh polymer screen and sintered (500 °C, 30 min). The carbon paste was screen printed using a 43 mesh polymer screen and sintered (500 °C, 30 min). Cell data presented in the Supporting Information was calculated from 12 devices with a single pixel in each device.

Perovskite Deposition: The substrates were then moved into a nitrogen glovebox. A 2 M solution of PbI₂ and PbBr₂ at ratio of 85:15 in a DMF:DMSO (85:15) mixture was prepared. About 2 µL of the solution was drop-casted onto the substrate active area, and annealed on a 70 °C for 30 min. The substrates were then dipped in a 0.06 M solution of FAI:MABr at a ratio of 85:15 in isopropyl alcohol for different times from 5 to 90 min, and then dipped in clean isopropyl alcohol for 5 s. Finally, the cells were annealed on a hot plate (70 °C) for 2 h.

PV Characterization: JV curves and standard PV properties were obtained using a Newport solar simulator system consisting of an Oriel I–V test station using an Oriel Sol3A simulator. The solar simulator was class AAA for spectral performance, uniformity of irradiance, and temporal stability. It is equipped with a 450 W xenon lamp. The output power was adjusted to match AM1.5 global sunlight (100 mW cm^{−2}). The spectral match classifications were IEC60904-9 2007, JIC C 8912, and ASTM E927-05. J–V curves were obtained by applying a varying external bias on the cell and measuring the generated photocurrent with a Keithley model 2400 digital source meter. The bias voltage was scanned from 1 to −0.1 V in steps of 10 mV with a dwell time of 40 ms at each step. The PV performance was measured using a mask with a window area of 0.085 cm². A silicon reference cell was used to calibrate the solar simulator. All PV measurements were carried out under ambient conditions in the air.

CE and IMVS: CE and IMVS were measured using Autolab Potentiostat-Galvanostat (PGSTAT) with a FRA32M LED driver equipped with a cool white light source. A Nova 2.1 software program was used to collect and analyze the obtained data. The CE measurement parameters used were as follows—discharge time of 2 s, illumination time of 5 s, delay times measured were 0.5, 0.6, 0.8, 1, 1.3, 1.61, 2, 2.5, 3.2, 4, 5, 6, 7, 8, 9, 10, 11, 12, 13, 14, and 15 s. The IMVS measurements were conducted by illuminating the sample at different light intensities, varying from 0.1 to 0.7 sun, with a sinusoidal wave modulation, with frequencies ranging from 1 Hz to 50 kHz. Lifetimes were calculated using the formula: $\tau = 1/(2\pi \cdot \text{frequency at a minimum of semicircle})$.

XRD: First, powder XRD characterization was measured on the full devices fabricated at the four different dipping times. The second characterization was measured on the same device in three stages—fresh, after 3 h illumination (Oriol Sol3A simulator) at open circuit, and after 1-day recovery in the dark. During that time, the device was kept under nitrogen environment, excluding the time of the XRD measurements. Immediately after each stage the device was taken for XRD measurements. All measurements were carried out using a D8 Advance diffractometer (Bruker AXS, Karlsruhe, Germany). The diffractometer was operated in grazing incidence X-ray diffraction (GIXRD) mode with a grazing incidence angle value of 2.5° . The diffractometer was equipped with a 217.5 mm radius goniometer, a secondary graphite monochromator, 2° Soller slits, and a 0.2 mm receiving slit. XRD patterns were recorded using Cu K α radiation (I 1/4 1.5418 Å) with a tube voltage of 40 kV and a tube current of 40 mA. A step-scan mode was used with a step size of $0.02^\circ 2\theta$, and a counting time of between 1 and 3 s per step. Measurements were carried out at room temperature.

Stability Measurements: All outdoor exposure experiments were conducted during clear sky day (10:00 a.m. to 14:00 p.m.) in Sede Boquer, Israel (latitude, 30.8°N ; longitude, 34.8°E ; altitude, 475 m). The sunlight spectrum measured in the daytime at Sede Boquer was very close to the AM1.5G spectrum.^[50] The cells used for stability studies were fabricated using the optimized procedure described above, with 20 min dipping. Some of the cells were sealed in an environmental box in the glovebox then the cells were exposed in outdoor natural sunlight through the glass substrate in N_2 environment. After the required time interval of exposure, the cells were taken inside the lab, the box opened, and $J-V$ measured in air. After the measurements, the box and cells were taken into the glovebox again and sealed in the glovebox and the process was repeated. Recovery occurred during dark storage under N_2 . Ambient-exposed cells were measured similarly without the box, and recovery occurred during storage in indoor lab ambient.

Supporting Information

Supporting Information is available from the Wiley Online Library or from the author.

Acknowledgements

L.E. thanks the Ministry of Energy and the Israel Science Foundation (grant no. 2552/17) for the financial support for this project. C.S.P. gratefully acknowledges support from BGU's Kreitman post-doctoral fellowship. This research was also supported by the Israel Science Foundation (grant no. 71/1271). L.E. and I.V.F. gratefully acknowledge support by Israel's Ministry of Energy (grant no. 215-11-037).

Conflict of Interest

The authors declare no conflict of interest.

Data Availability Statement

Research data are not shared.

Keywords

dipping times, mesoporous carbon cells, perovskites, stabilities, two-step deposition

Received: January 11, 2021

Published online:

- [1] T. Miyasaka, A. Kojima, K. Teshima, Y. Shirai, *J. Am. Chem. Soc.* **2009**, *131*, 6050.
- [2] D. B. Mitzi, *Inorg. Chem.* **2000**, *39*, 6107.
- [3] M. M. Lee, J. Teuscher, T. Miyasaka, T. N. Murakami, H. J. Snaith, *Science* **2012**, *338*, 643.
- [4] C. Roldán-Carmona, O. Malinkiewicz, R. Betancur, G. Longo, C. Mombona, F. Jaramillo, L. Camacho, H. J. Bolink, *Energy Environ. Sci.* **2014**, *7*, 2968.
- [5] S. D. Stranks, G. E. Eperon, G. Grancini, C. Menelaou, M. J. Alcocer, T. Leijtens, L. M. Herz, A. Petrozza, H. J. Snaith, *Science* **2013**, *342*, 341.
- [6] A. M. Leguy, P. Azarhoosh, M. I. Alonso, M. Campoy-Quiles, O. J. Weber, J. Yao, D. Bryant, M. T. Weller, J. Nelson, A. Walsh, M. Van Schilfgaarde, *Nanoscale* **2016**, *8*, 6317.
- [7] M. Liu, M. B. Johnston, H. J. Snaith, *Nature* **2013**, *501*, 395.
- [8] J. Y. Jeng, Y. F. Chiang, M. H. Lee, S. R. Peng, T. F. Guo, P. Chen, T. C. Wen, *Adv. Mater.* **2013**, *25*, 3727.
- [9] L. Etgar, P. Gao, Z. Xue, Q. Peng, A. K. Chandiran, B. Liu, M. K. Nazeeruddin, M. Grätzel, *J. Am. Chem. Soc.* **2012**, *134*, 17396.
- [10] Z. Ku, Y. Rong, M. Xu, T. Liu, H. Han, *Sci. Rep.* **2013**, *3*, 1.
- [11] Y. Rong, Y. Hu, A. Mei, H. Tan, M. I. Saidaminov, S. I. Seok, M. D. McGehee, E. H. Sargent, H. Han, *Science* **2018**, *6408*, 361.
- [12] C. C. Boyd, R. Cheacharoen, K. A. Bush, R. Prasanna, T. Leijtens, M. D. McGehee, *ACS Energy Lett.* **2018**, *3*, 1772.
- [13] K. Domanski, J. P. Correa-Baena, N. Mine, M. K. Nazeeruddin, A. Abate, M. Saliba, W. Tress, A. Hagfeldt, M. Grätzel, *ACS Nano* **2016**, *10*, 6306.
- [14] S. He, L. Qiu, L. K. Ono, Y. Qi, *Mater. Sci. Eng. R: Rep.* **2020**, *140*, 100545.
- [15] S. G. Hashmi, A. Tihoonen, D. Martineau, M. Ozkan, P. Vivo, K. Kaunisto, V. Ulla, S. M. Zakeeruddin, M. Grätzel, *J. Mater. Chem. A* **2017**, *5*, 4797.
- [16] X. Li, M. Tschumi, H. Han, S. S. Babkair, R. A. Alzubaydi, A. A. Ansari, S. S. Habib, M. K. Nazeeruddin, S. M. Zakeeruddin, M. Grätzel, *Energy Technol.* **2015**, *3*, 551.
- [17] Y. Hu, S. Si, A. Mei, Y. Rong, H. Liu, X. Li, H. Han, *Sol. RRL* **2017**, *1*, 1600019.
- [18] G. Grancini, C. Roldán-Carmona, I. Zimmermann, E. Mosconi, X. Lee, D. Martineau, S. Narbey, F. Oswald, F. De Angelis, M. Graetzel, M. K. Nazeeruddin, *Nat. Commun.* **2017**, *8*, 1.
- [19] Q. Wang, W. Zhang, Z. Zhang, S. Liu, J. Wu, Y. Guan, A. Mei, Y. Rong, Y. Hu, H. Han, *Adv. Energy Mater.* **2020**, *10*, 1.
- [20] J. Wu, W. Zhang, Q. Wang, S. Liu, J. Du, A. Mei, Y. Rong, Y. Hu, H. Han, *J. Mater. Chem. A* **2020**, *8*, 11148.
- [21] A. Mei, X. Li, L. Liu, Z. Ku, T. Liu, Y. Rong, M. Xu, M. Hu, J. Chen, Y. Yang, M. Grätzel, *Science* **2014**, *345*, 295.
- [22] Y. Hu, Z. Zhang, A. Mei, Y. Jiang, X. Hou, Q. Wang, K. Du, Y. Rong, Y. Zhou, G. Xu, H. Han, *Adv. Mater.* **2018**, *30*, 1.

- [23] X. Hou, M. Xu, C. Tong, W. Ji, Z. Fu, Z. Wan, F. Hao, Y. Ming, S. Liu, Y. Hu, H. Han, *J. Power Sources* **2019**, 415, 105.
- [24] J. Chen, Y. Xiong, Y. Rong, A. Mei, Y. Sheng, P. Jiang, Y. Hu, X. Li, H. Han, *Nano Energy* **2016**, 27, 130.
- [25] K. Liang, D. B. Mitzi, M. T. Prikas, *Chem. Mater.* **1998**, 10, 403.
- [26] J. Burschka, N. Pellet, S. J. Moon, R. Humphry-Baker, P. Gao, M. K. Nazeeruddin, M. Grätzel, *Nature* **2013**, 499, 316.
- [27] S. G. Hashmi, D. Martineau, X. Li, M. Ozkan, A. Tiihonen, M. I. Dar, T. Sarikka, S. M. Zakeeruddin, J. Paltakari, P. D. Lund, M. Grätzel, *Adv. Mater. Technol.* **2017**, 2, 1600183.
- [28] A. Schneider, S. Alon, L. Etgar, *Energy Technol.* **2019**, 7, 1900481.
- [29] H. Min, L. Linfeng, M. Anyi, Y. Ying, L. Tongfa, H. Hongwei, *J. Mater. Chem. A* **2014**, 2, 17115.
- [30] H. Abdy, Z. Heydari, A. Aletayeb, M. Kolahdouz, E. Asl-Soleimani, *J. Mater. Sci.: Mater. Electron.* **2020**.
- [31] M. Wang, Y. Feng, J. Bian, H. Liu, Y. Shi, *Chem. Phys. Lett.* **2017**, 692.
- [32] X. Duan, X. Li, L. Tan, Z. Huang, J. Yang, G. Liu, Z. Lin, Y. Chen, *Adv. Mater.* **2020**, 32, 2000617.
- [33] L. Qiu, J. Zou, W. Chen, L. Dong, D. Mei, L. Song, J. Wang, P. Jiang, P. Du, J. Xiong, *Sustainable Energy Fuels* **2021**, 5, 469.
- [34] B. Li, J. Shi, J. Lu, W. L. Tan, W. Yin, J. Sun, L. Jiang, R. T. Jones, P. Pigram, C. R. McNeill, Y. Cheng, J. J. Jasieniak, *ACS Appl. Energy Mater.* **2020**, 3, 3358.
- [35] S. Shahbazi, M. Li, A. Fathi, E. W. Diau, *ACS Energy Lett.* **2020**, 5, 2508.
- [36] S. Wang, W. Shen, Y. Chu, W. Zhang, L. Hong, A. Mei, Y. Rong, Y. Tang, Y. Hu, H. Han, *J. Phys. Chem. Lett.* **2020**, 11, 9689.
- [37] N. J. Jeon, J. H. Noh, W. S. Yang, Y. C. Kim, S. Ryu, J. Seo, S. I. Seok, *Nature* **2015**, 517, 476.
- [38] P. Gratia, G. Grancini, J. N. Audinot, X. Jeanbourquin, E. Mosconi, I. Zimmermann, D. Dowsett, Y. Lee, M. Grätzel, F. De Angelis, K. K. Sivula, *J. Am. Chem. Soc.* **2016**, 138, 15821.
- [39] H. F. Zarick, N. Soetan, W. R. Erwin, R. Bardhan, *J. Mater. Chem. A* **2018**, 5507.
- [40] E. Mosconi, A. Amat, M. K. Nazeeruddin, M. Grätzel, F. De Angelis, *J. Phys. Chem. C* **2013**, 117, 13902.
- [41] Y. Galagan, E. W. C. Coenen, W. J. H. Verhees, R. Andriessen, *J. Mater. Chem. A* **2016**, 4, 5700.
- [42] E. Avigad, L. Etgar, *ACS Energy Lett.* **2018**, 3, 2240.
- [43] Y. C. Kim, N. J. Jeon, J. H. Noh, W. S. Yang, J. Seo, J. S. Yun, A. Ho-Baillie, S. Huang, M. A. Green, J. Seidel, T. K. Ahn, *Adv. Energy Mater.* **2016**, 6, 1502104.
- [44] B. W. Park, N. Kedem, M. Kulbak, W. S. Yang, N. J. Jeon, J. Seo, G. Kim, K. J. Kim, T. J. Shin, G. Hodes, D. Cahen, *Nat. Commun.* **2018**, 9, 1.
- [45] M. Saliba, T. Matsui, J. Y. Seo, K. Domanski, J. P. Correa-Baena, M. K. Nazeeruddin, S. M. Zakeeruddin, W. Tress, A. Abate, A. Hagfeldt, M. Grätzel, *Energy Environ. Sci.* **2016**, 9, 1989.
- [46] E. V. Péan, C. S. De Castro, S. Dimitrov, F. De Rossi, S. Meroni, J. Baker, T. Watson, M. L. Davies, *Adv. Funct. Mater.* **2020**, 30, 1909839.
- [47] F. De Rossi, J. Barbé, D. M. Tanenbaum, L. Cinà, L. A. Castriotta, V. Stoichkov, Z. Wei, W. C. Tsoi, J. Kettle, A. Sadula, J. Chircop, *Energy Technol.* **2020**, 8, 2000134.
- [48] M. V. Khenkin, A. KM, I. Visoly-Fisher, S. Kolusheva, Y. Galagan, F. Di Giacomo, O. Vukovic, B. R. Patil, G. Sherafatipour, V. Turkovic, H. G. Rubahn, *ACS Appl. Energy Mater.* **2018**, 1, 799.
- [49] C. Zhu, X. Niu, Y. Fu, N. Li, C. Hu, Y. Chen, X. He, G. Na, P. Liu, H. Zai, Y. Ge, *Nat. Commun.* **2019**, 10, 1.
- [50] N. Rolston, K. A. Bush, A. D. Printz, A. Gold-Parker, Y. Ding, M. F. Toney, M. D. McGehee, R. H. Dauskardt, *Adv. Energy Mater.* **2018**, 8, 1802139.
- [51] Y. Rakita, I. Lubomirsky, D. Cahen, *Mater. Horizons* **2019**, 6, 1297.
- [52] D. R. Ceratti, Y. Rakita, L. Cremonesi, R. Tenne, V. Kalchenko, M. Elbaum, D. Oron, M. A. C. Potenza, G. Hodes, D. Cahen, *Adv. Mater.* **2018**, 30, 1706273.
- [53] S. G. Hashmi, D. Martineau, M. I. Dar, T. T. Myllymäki, T. Sarikka, V. Ulla, S. M. Zakeeruddin, M. Grätzel, *J. Mater. Chem. A* **2017**, 5, 12060.
- [54] M. V. Khenkin, E. A. Katz, A. Abate, G. Bardizza, J. J. Berry, C. Brabec, F. Brunetti, V. Bulović, Q. Burlingame, A. Di Carlo, R. Cheacharoen, *Nat. Energy* **2020**, 5, 35.
- [55] D. Berman, D. Faiman, *Sol. Energy Mater. Sol. Cells* **1997**, 45, 401.